Author/s:
Chambers, CRS;Brassington, GB;Simmonds, I;Walsh, K

Title:
Precipitation changes due to the introduction of eddy-resolved sea surface temperatures into simulations of the "Pasha Bulker" Australian east coast low of June 2007

Date:
2014-04-05

Citation:
Chambers, C. R. S., Brassington, G. B., Simmonds, I. & Walsh, K. (2014). Precipitation changes due to the introduction of eddy-resolved sea surface temperatures into simulations of the "Pasha Bulker" Australian east coast low of June 2007. Meteorology and Atmospheric Physics, 125 (1-2), pp.1-15. https://doi.org/10.1007/s00703-014-0318-4.

Persistent Link:
https://hdl.handle.net/11343/282792

Precipitation Changes Due to the Introduction of Eddy-Resolved Sea Surface Temperatures into Simulations of the "Pasha Bulker" Australian East Coast Low of June 2007

Christopher R. S. Chambers

School of Earth Sciences, University of Melbourne, Parkville, Australia

Gary B. Brassington

Centre for Australian Weather and Climate Research, Bureau of Meteorology, Sydney, Australia

Ian Simmonds

School of Earth Sciences, University of Melbourne, Parkville, Australia

Kevin Walsh

School of Earth Sciences, University of Melbourne, Parkville, Australia

Corresponding author address: Christopher Chambers, 700 Collins St, Docklands, VIC 3008, Australia.

E-mail: c.chambers@bom.gov.au

Tel: 61 (0)3 9669 4614

Abstract

Weather Research and Forecast (WRF) model simulations are used to investigate how the distribution of precipitation is related to the distribution of sea surface temperatures (SSTs) during the life cycle of the Australian east coast low of 7-9 June 2007. The focus is placed on investigating changes caused by the introduction of complex ocean eddy and filament structures present in the Bluelink reanalysis (BRAN) SST dataset. In the simulations, enhancement of rainfall is found over and downwind of warmer SSTs and suppression of rainfall over and downwind of cooler SSTs. Specifically, a large warm eddy present during this case is associated with an enhancement of rainfall along its downwind (southern) flank where a strong SST gradient exists. Overall, the model demonstrates considerable skill in simulating the event, although the simulated main rainband propagates southward earlier than observed. However the maximum one-hourly rainfall totals at the stations that received the greatest rainfall are greater and closer to the observed maxima when the BRAN SSTs are used. Global Position and Tracking System (GPATS) lightning data are overlaid on maps of SST and used to investigate whether a thunderstorm-SST relationship is discernable. An ensemble of WRF simulations are used to establish what atmospheric changes contribute to the observed distributions of thunderstorms. It is concluded that the complex upper ocean heat content structure present during this case significantly influenced the storm's impact. Therefore an accurate eddy resolving SST dataset may be important for accurate forecasts of future storms of similar nature.

1. Introduction

On 7 and 8 June 2007 a low pressure system off the coast of New South Wales (NSW), Australia (Fig. 1) led to nine fatalities, major flooding, record waves, AU$1.5 billion in damage, and to the grounding of the 76,000 tonne bulk ore carrier Pasha Bulker on Nobbys Beach in Newcastle (Mills et al. 2010). The low was characterised by a persistent wide band of strong onshore winds on its southern side that was responsible for the generation of a record swell, with the Sydney Waverider Buoy (at the time approximately 120 km from the storm centre) recording a maximum wave height of 14.1 m. At the same time, a long lasting, slowly southward propagating, east-west oriented thunderstorm rainband moved onshore in the Newcastle area leading to very high and localized rainfall. Within this rainband, an intense mesoscale low pressure developed offshore and moved onshore at 1500 UTC 8 June. A comprehensive study of both the large scale and localised elements of the storm is found in Mills et al. (2010).

This low pressure system falls into the category of storms known as Australian east coast lows (ECLs) or east coast cyclones (Bridgman 1985, Holland et al. 1987, McInnes et al. 1992, Qi et al. 2006, Browning and Goodwin 2013, Dowdy et al. 2013a, b). These are subtropical low pressure weather systems that tend to develop rapidly over the oceanic region where the warm East Australian Current (EAC) flows southward off the east coast of Australia. Subtropical storms such as ECLs can have characteristics of both tropical and extratropical cyclones (Evans and Guishard 2009) and as such are thought to be hybrid storms that develop through both baroclinic instability and diabatic heating related instabilities (Hart 2003). They have a large range of sizes from 50 to 1000 km and can last for a few hours to several days. On average there are ten per year and they typically occur over the autumn and winter months, with a peak in activity in June (Hopkins and Holland 1997).

On the large scale, ECLs typically develop from consistent upper and lower level atmospheric patterns. The lower-atmospheric pattern is a low or trough in the subtropical easterly flow known as an “easterly dip” (Fandry and Leslie 1984) that has a ridge on its poleward side. These features in the surface pressure pattern can be seen at 1200 UTC 8 June 2007 in Fig. 1. This pattern tends to be associated with increase low level moisture and temperature due to advection from more tropical latitudes and through surface ocean fluxes enhanced by the strong winds. These “easterly dips” develop under, or downstream of, a mid-tropospheric cold core cyclone that originates as a cut-off low in the upper tropospheric westerlies. As this cold core cyclone moves eastward, it passes from over the dry air mass of continental Australia to over the warm moist air mass present over the warm waters of the EAC. Consequently, vertical instability rapidly increases as the upper low reaches the east Australian coast.

The name east coast low implies that there are critical geographically stationary or quasi-stationary features that cause the Australian east coast to be especially favourable for the formation of these storms. The prime candidates (as shown in Fig. 2) are: 1) the large dry continental region to the west 2) the Great Dividing Range of mountains close to the east coast and 3) the character of the EAC. The mountains of east Australia have been shown to play a role in the formation of the trough associated with easterly dips (Fandry and Leslie 1984). It is also well known that flow across a mountain range can induce vortex stretching on the lee side and lead to the formation of surface low pressure (e.g. Holton 1992). Leslie et al. (1987) showed that the mountains can also deflect low-level easterly flow cyclonically and act as a focus for moist ascent. While these and other factors are important for ECL formation, this study focuses on the role of complex thermal features in the EAC.

The EAC is a western boundary current of the South Pacific sub-tropical gyre that propagates poleward along the edge of the continental shelf of the east coast of Australia

from the bifurcation point of the South Equatorial Current between 14°-18°S (Church, 1987) to a separation point located on average at ~32°S (Godfrey et al. 1980). The EAC transports warm tropical water from the Coral Sea poleward to the Tasman Sea. The EAC has a much greater eddy kinetic energy than other western boundary currents e.g., the Gulf Stream (Hamon 1965; Stammer 1997; Brassington et al. 2011). Anticyclonic eddies of the order of 250 km diameter are shed from the current at the separation point. As warm eddies or current filaments move southward they enter a progressively cooler ocean environment. The warm eddies can have a mixed layer depth extending to over 300 m in their core (Andrews and Scully-Power 1976) and their rotation and deep vertical structure resists cooling of the eddy interior. As a consequence, regions of large sea surface temperature (SST) gradients can develop and maintain themselves off the east coast south of 35°S along the edges of these warm eddies as these two ocean masses collide (Andrews 1979).

SST gradients have been found to impact the marine atmospheric boundary layer in a number of ways. A strong positive correlation between SST and surface wind speed perturbations is found at spatial scales of between 100 and 1000 km (see the review by Small et al. 2008) in regions with large SST gradients. Sweet et al. (1981) attributed a positive correlation between SST and surface wind speed to increased atmospheric instability over warmer waters, inducing downward momentum transfer from the stronger winds aloft. Alternatively Huang and Raman (1988) showed the importance of pressure-driven flows in this SST – wind interaction. A surface wind convergence zone along the Gulf Stream was found by Raman and Riordan (1988) and Warner et al. (1990) found that this convergence zone is caused by sharp SST gradients associated with the current. Hobbs (1987) introduced the concept of a 'Gulf Stream Rainband' based on in situ observations of a rainband over the north wall of the Gulf Stream. This rainband has been associated with rapidly developing thunderstorms (Trunk and Bosart 1990, Christian et al. 2003, Li et al. 2004). Kuwano-

Yoshida et al. (2010) found convective precipitation to be sensitive to the strength of the SST gradients along the Gulf Stream while Skyllingstad and Edson (2009) showed that in a cold air outbreak, stronger precipitation occurred in a simulation with an SST front than in a case with constant SST. Improved precipitation distribution was also found by Maeda et al. (2011) for wintertime over the East China Sea when an ocean eddy resolving SST dataset was used and Li et al. (2014) showed that an eddy resolving SST was vital to regional climate downscaling in the California region. The relationship between deep convection and warm current SST distributions has also been investigated for the Kuroshio (e.g. Xie et al. 2002) and Agulhas return (Liu et al. 2007) currents. In the Kuroshio Extension region, Putrasahan et al. (2013) found precipitation anomalies to be forced by mesoscale SST gradients. Similar studies have not been performed for the EAC, however.

In addition to the case studied here, four other ECLs occurred off the NSW coast during June 2007, making it one of the most active months on record. An unusually large warm ocean eddy was present in the region during this month. It is the goal of this study to determine in what ways the fine scale structure of this eddy influenced the precipitation in the simulated storm.

The investigation is presented as follows. Section 2 describes the data and methodology used, while section 3 provides an overview of the event based on the model results and a comparison of the model rainfall and four observational stations is made. Section 4 examines the sensitivity of the model rainfall to the SST input data and the model results are considered in relation to the observed distribution of lightning. A discussion of the results is in section 5 followed by the study conclusions in section 6.

2. Method

The 7/8 June 2007 ECL is simulated using the Weather Research and Forecast (WRF) Model (Skamarock et al. 2005) version 3.3.1. Two domains on a Lambert conformal grid, with resolutions of 15 and 3 km respectively, are used for the simulations located as shown on Fig. 2. The outer domain (domain 1) is 221 by 171 grid points (3315 km by 2565 km) and the inner domain (domain 2) is 301 by 261 grid points (903 km by 783 km). Fifty five levels are used in the vertical with a model top at 30 hPa. The atmospheric initialisation data comes from the 1 degree National Centers for Environmental Prediction (NCEP) Final Analysis dataset (Global Climate and Weather Modeling Branch 2003). The 30-s resolution U.S. Geological Survey (USGS) terrestrial data are used for the terrain specification.

The Thompson et al. (2004) microphysics scheme is used, which contains six water classes (water vapor, cloud water, rain, snow, graupel, and cloud ice). The Betts-Miller-Janjic (Betts 1986; Betts and Miller 1986; Janjic 1994) cumulus scheme is used on domain 1 but not on domain 2 where the resolution is considered high enough for the convection to be resolved explicitly. The Yonsei University planetary boundary layer parameterisation is used with the Monin–Obukhov surface layer scheme (Hong et al. 2006). Radiative effects are parameterised using the Dudhia (1989) short wave radiation scheme and the Rapid Radiative Transfer Model (RRTM) for long wave radiation with six molecular species (Mlawer et al. 1997).

Three simulations are conducted that are identical except for the SST data used as input. The simulations and SST configurations are summarised in Table 1. For all cases the SSTs evolve on a 6 hourly basis. The first of the SST configurations (Skin) is the 1 degree resolution skin temperature from the NCEP FNL (Final) Operational Global Analysis data that are derived from the Global Data Assimilation System (GDAS). This is the least detailed of the three datasets and, as Fig. 3a shows, has an absence of any eddy variability in the EAC

on domain 2. This dataset is used as a comparison with the more detailed datasets as it generally contains a smoothed pattern with weaker SST gradients.

The control case (Control) uses daily 0.5 degree NCEP Real-Time SST data (Thiebaux et al. 2003) which employs a two-dimensional variational interpolation analysis of the most recent buoy, ship, and satellite-retrieved SST data (Fig. 3b). This is a daily dataset which is then time-interpolated down to 6 hourly periods during the pre-processing stage of WRF to be consistent with the input atmospheric data. This dataset is commonly used in WRF simulations to improve the SST initialization over that provided by the atmospheric dataset such as the NCEP skin temperatures.

The Bluelink ReANalysis (BRAN, Schiller et al. 2008) case uses SST data from an eddy resolving ocean model simulation using the Modular Ocean Model (MOM, Griffies et al. 2004) which is constrained through the data assimilation of altimetry, SST and in situ profiles using the Bluelink Ocean Data Assimilation System (BODAS, Oke et al. 2008). Eddy resolving simulations with data assimilation have been found to markedly improve features of the circulation in the Pacific compared to coarser resolution models (You and Yoon 2010). The BRAN output data is daily-averaged and is therefore time-interpolated to be 6 hourly to fit with the atmospheric initial conditions. In an Australian centred region (90°E-180°E, 75°S-16°N) the BRAN data has a resolution of 0.1 degrees, and the WRF model domains we used here are within this region. The BRAN data contains more complex SST structures in the EAC than the two NCEP datasets, with mesoscale filaments and eddies present, as can be seen on Fig. 3c. It is used here to determine if the presence of these complex ocean surface structures produce a clear effect on the precipitation during this storm simulation when compared with the other initializations.

The Commonwealth Scientific and Industrial Research Organisation (CSIRO) Atlas of Regional Seas (CARS, Ridgway et al. 2002) climatological SSTs are used to calculate

anomalies for the initial time of each case as shown on Fig. 3d, e, and f. In Control and BRAN the warm eddy contains warmer SSTs than the climatological values for the initial time whereas the cooler eddies to the south and east are cooler than the climatology. The average SSTs over the simulation period area-averaged over domain 2 are 21.15, 21.58, and 21.35 °C for the Control, BRAN and Skin runs respectively, indicating that the averaged SSTs are within 0.5 °C of each other in this region.

Over the 60-hour period covered by the simulations only small changes occur to the SST distribution. As an example the start and end SST for the BRAN case is plotted on Fig. 4. Some cooling is evident over the period, for example to the south of the main warm eddy at 153° E, 34° S, but the general distribution remains similar and the central warm eddy retains its structure over the 60 hour period. Interestingly it can be seen that the cooling occurs south of the warm eddy whereas the warm eddy approximately retains its surface temperatures and in fact appears to warm slightly in some areas. This change over the course of the simulation is responsible for an increase in the SST gradient along the southern flank of the warm eddy.

To test the statistical robustness of the simulation results, two extra cases for both BRAN and Skin have been run with different initialization times to form, for these two cases, a 3-member lagged ensemble. The ensemble for each SST initialisation consists of 1) the original run (BRAN or Skin), 2) domain 2 initialised 6 hours later (BRAN6 or Skin6), and 3) domain 2 initialized 12 hours later (BRAN12 or Skin12) than domain 1.

3. Overview and observational comparison

As outlined in Mills et al. (2010) the ECL was preceded by a pronounced middle tropospheric cold core cyclone. Fig. 5 shows the progression of this feature at 500 hPa on domain 1 over the first 48 hours of the Control simulation. The mid-level low progresses eastward towards

the coast, with warming occurring as it crosses the coast and moves offshore. At the surface over the same period a quasi-stationary low pressure deepens near the east coast as shown in Fig. 6. Consequently the westward tilt at the beginning of the period disappears by the end, strongly suggestive of a shift from baroclinic to barotropic processes being dominant.

A tight pressure gradient developed on the southern side of the low leading to a persistent fetch of strong east-south-easterly winds. The pressure gradient was enhanced by an eastward propagating high pressure west of Tasmania. While Fig. 6 indicates minimum sea level pressures above 1000 hPa, localised regions of lower pressures were simulated leading to an overall simulation minimum of 996 hPa on domain 2 at 0300 UTC 8 June for the Control case, as shown in Fig. 7.

To investigate the accuracy of the simulated rainfall, a comparison between modelled rainfall and rain gauge observations is presented here for four coastal observation stations. This analysis considers the 48 hour period from 0000 UTC 7 June to 0000 UTC 9 June 2007 beginning after the first 12 hours of the simulation are ignored to account for model spin up. The four observation stations have been chosen to allow for a comparison between the model and observed one hourly rainfall total: two stations, Newcastle Nobbys Signal Station Automatic Weather Station (hereafter Nobbys) and Williamtown Royal Australian Air Force (hereafter Williamtown), are within the area of greatest impact, while one station, Coffs Harbour Meteorological Office (hereafter Coffs Harbour), is well to the north and one station, Sydney Observatory Hill (hereafter Sydney) is to the south (see Fig. 4 for locations on domain 2).

All the simulations produced a peak in one hourly rain accumulations around 6 hours before the observed peak at Nobbys (Fig. 8a). This error occurs because the model propagates the main rain band southward earlier than observed. The simulated peak rainfall period also has a shorter duration (6 hours) compared with observed (10 hours). Comparing the three

simulations, it is apparent that the BRAN case produces the largest one hourly rainfall totals with the largest being 39 mm, somewhat greater than the 29 and 17 mm seen in Control and Skin, respectively. For Williamtown (Fig. 8b) the peak simulated rainfall again precedes the observed peak and the largest one hourly total occurs in the BRAN case. All simulations failed to capture the observed peak of 45.8 mm that fell in the hour ending at 0300 UTC 8 June.

The Coffs Harbour observations (not shown) confirm that both the simulated and observed rainfall totals were low to the north of the rain band. For Sydney (Fig. 8c) the simulated rainfall totals considerably exceed the observed rain apart from in the final 12 hours. Again the southward propagated rainband is responsible for the earlier and greater peak in the simulations. Of significance are the greater maximum one hourly rainfall totals in the Control and Skin cases over the BRAN case. This results in the BRAN case simulating maximum one hourly rainfall closer to observed. These results will be shown in the following section to be a signature of rainfall suppression in the BRAN case due to the large area of cooler SSTs offshore of this region shown in Fig. 4. The 48 hour total rainfall, shown in the top right of each graph on Fig. 8, indicates that at all of these stations BRAN produced the most accurate total rainfall and Skin the least accurate.

Fig. 9 shows how the distribution of 24 hour rainfall was affected by changing the SST and how the distribution compared to the observed distribution. During the first 24 hour period a localized region of rain from 50 to over 150 mm can be seen in the vicinity of the Williamtown and Nobbys stations in BRAN (Fig. 9a), however in the Skin run (Fig. 9b) there is less rain (25 to 50 mm) over the stations. Nonetheless there is a larger region over land of over 50 mm of rain in Skin than in BRAN with greater rainfall in Skin particularly apparent to the north of Williamtown. In the second 24 hour period the BRAN case shows a highly localized band of over 50 mm rain remaining over Nobbys whereas in Skin the area of over

50 mm is located just south of Nobbys. BRAN has more focussed and higher rainfall near 33.5° S, 150.5° E than Skin. BRAN therefore appears to be a closer match to the observed rainfall distribution during this period with rainfall totals of over 200 mm occurring over a larger area than in Skin. It is clear that these are quite localized features and so in the following section we establish how the differences in rainfall relate to the differences in SST.

4. Rainfall distribution sensitivity to SST

To further investigate the sensitivity of precipitation to changes in SST boundary conditions, time-averaged difference plots are utilised. Differences in rainfall totals are calculated between the most detailed SST dataset run (BRAN) and the least detailed (Skin) of the original non-ensemble runs. The post spin-up 48 hour period (0000 UTC 7 June to 0000 UTC 9 June) of the simulations is used for this analysis. The 48 hour averaged SST difference (BRAN – Skin) is plotted in Fig. 10. This shows that the warm eddy resolved by the BRAN data contains higher SSTs than the Skin run, but that the waters south of the eddy are colder in the BRAN data. The strong SST gradient along the southern edge of the warm eddy in the BRAN data is also evident in this difference plot.

The 48 hour rainfall difference (BRAN – Skin), plotted on Fig. 11, shows that an enhancement of rainfall in the BRAN case occurs along the southern edge of the warm eddy. The 48 hour average wind vectors shown on this plot indicate that this rainfall enhancement occurs on the downwind edge of the warm eddy from 33° S, 153° E to 34° S, 156° E. Local enhancements in the BRAN case over the Skin case in this region exceed 100 mm. South of this, rainfall is suppressed in the BRAN simulation over and downwind of the cooler SSTs associated with the cold eddy. These patterns of enhanced/suppressed rainfall downwind of warm/cold anomalies in the BRAN run can be seen to apply to other regions over the domain (e.g. enhanced at 30° S, 156.5° E, 34° S, 158.5° E, and 35.5° S, 154.5° E, suppressed at 33°

S, 157° E, 34.5° S, 157.5° E, and 33.5° S, 152.5° E). In the strongest low level flow south of 35 °S, the rainfall anomalies appear to have been advected further downstream of the SST anomalies than elsewhere.

To determine the changes over a shorter time-scale, the four 12-hourly rainfall total differences of the 48 hour analysis period are plotted in Fig. 12. The largest differences between the two initialisations occur within the southward propagating rainband. While some features appear to be stochastic and not related to the SST change, others exhibit a clear relationship to it. The most prominent feature occurs in Fig. 12b as the rainband passes over the region of strong SST gradients on the southern flank of the warm eddy. In this period a local enhancement of rainfall of 50 to 100 mm can be seen over the strong SST gradients. After this period a band of enhanced rainfall in the BRAN case occurs to the south of a band of reduced rainfall. This is an indication that the BRAN simulation propagates the rainband more quickly southward than the Skin case.

Fig. 12b also shows localised regions of enhanced and suppressed rainfall over the coast near 33 °S. The enhanced rainfall region lies over the Nobbys and Williamtown rainfall stations. This feature explains the larger 1 hourly rainfall totals seen during this period in the BRAN simulation seen in Fig. 8. Fig. 12c shows a region of suppressed rainfall in the BRAN simulation occurs over the Sydney region. This suppression explains the large discrepancy in rainfall between the BRAN and Skin (and Control) simulations during this period shown in Fig. 8c.

To obtain an estimate of the robustness of these simulated structures, our ensemble simulations are used to explore the distribution of rain when an average over the three simulations is considered. The average 48 hour rainfall totals across the three ensemble forecast simulations for the BRAN and Skin initialisations is plotted on Fig. 13. The regional rainfall pattern appears to be in broad agreement between the cases with the heaviest rainfall

occurring over the land between 33 and 34 °S. The local patterns, however, exhibit some clear differences that are best visualised by again plotting the 48 hour rainfall differences.

Fig. 14 shows that the three-member lagged ensemble 48 hour rainfall differences exhibit a similar but smoother pattern compared with Fig. 11, indicating there is a stochastic component. This agreement also indicates, however, that the broad-scale pattern is statistically robust. In particular the enhancement of rain along the southern edge of the warm eddy and suppression over and downwind of the warm eddy to the south seen in Fig. 4 remain clear in the three member ensemble.

To further expand the investigation into the distribution of precipitation during this storm, the sensitivity of convective available potential energy (CAPE) to SST input data is investigated and considered in relation to the observed distribution of lightning. It is known that a band of thunderstorms impacted the Newcastle area, and that this band was largely responsible for the large rainfall totals (Mills et al. 2010). Lightning data is a useful source of information for the location of thunderstorms particularly in remote ocean areas that are partially or totally beyond the range of weather radar. Larger CAPE is associated with more vigorous convection which promotes more lightning (Williams et al. 1992; Rutledge et al. 1992). Additionally several studies have found correlations between lightning and precipitation rate (Alexander et al 1999; Chang et al. 2001; Pessi and Businger 2009). With these findings in mind we use the lightning data to compare with the model data to investigate whether the distribution of the thunderstorm related rainfall is sensitive to the SST initialisation.

The lightning data are obtained from the Global Position and Tracking System (GPATS 2013). GPATS data requires the arrival time of a lightning discharge to be recorded at three or more radio receivers (Cummins and Murphy 2009). This allows for the detection of return strikes and hence the ability to distinguish between cloud-to-cloud and cloud-to-

surface lightning. The analysis conducted here concentrates on lightning strike locations over the model analysis period.

All lightning strike locations for the entire 48 hour analysis period are plotted on Fig. 15. The overall pattern shows a concentration of lightning over and south of, the warm eddy with the particularly pronounced area of strikes over the coast in the Newcastle region near 33 °S, 152 °E. This can be compared with the 48 hour total CAPE for the BRAN and Skin cases and the CAPE difference, shown in Fig. 16. This shows the overall high CAPE throughout the region in both cases in a broad arc following the cyclonic flow. The differences between the cases can be seen to be directly related to the SST in each case with more variability in CAPE within the high CAPE arc in the BRAN run associated with the more complex and variable SST structures. The CAPE differences in Fig. 16c show this more clearly with reduced CAPE over the cool tongue east of the warm eddy and increased CAPE over the warm eddy, particularly along the southern flank.

By comparing Fig. 16c with the 48 hour rainfall total differences on Fig. 11 it can be seen that the enhancement of rain on the southern flank of the warm eddy is collocated with the largest positive CAPE differences. It is therefore likely that the enhanced rainfall in this region in the BRAN simulation was related to increased atmospheric thermal instability associated with the central warm eddy and the SST gradient along its southern edge. Other areas of enhanced rainfall also appear to be related to regions of enhanced CAPE such as near 30 °S 157 °E, 34 °S 159 °E, and 35 °S 155 °E. In fact it might be suspected that increased rainfall would show a greater relationship with regions of downwind CAPE decreases because this could indicate that the CAPE had been released in deep convection. By comparing the enhanced rainfall regions highlighted above there is indeed some indication of rainfall enhancement occurring on the downwind side of the elevated CAPE regions though further analysis will be required to confirm this relationship.

5. Discussion

The simulations presented here provide a new view of the impact that complex, high-resolution SST patterns can have on precipitation on short space and time scales during an Australian ECL. There are some significant errors when the simulations are compared with observations that are primarily caused by an earlier simulated southward propagation of the main rainband. Consequently there is an earlier rainfall maximum in the simulations than observed over the area of greatest rain. Of potential significance are the larger, and closer to observed, one hourly rainfall maxima seen in the BRAN simulations at both Nobbys and Williamtown (Fig. 8). This signal can be seen on Fig. 11 as an area of enhanced rainfall spreading westward from the warm eddy towards the coastline in this region. Mills et al. (2010) showed (their Figure 6) that the very large rainfall totals during this case were highly localised. Lightning data in Fig. 15 show a plume of lightning originating over the region of strong SST gradients. Since the model results suggest this region may be more favourable for thunderstorms in the BRAN simulations through increased CAPE (Fig. 16c), it could well be the case that this highly significant storm feature was directly triggered by the warm eddy and associated strong SST gradient. Given that the results here show that a strong SST gradient offshore will tend to focus and increase precipitation, it follows that this SST distribution must be considered as an important contributor to, and potential trigger for, the localised observed coastal rainfall. Nonetheless, the overall total rainfall of the ensemble on Fig. 11 indicates that the broad-scale rainfall pattern was similar in the Skin and BRAN runs. This is an indication that changing the SST did not produce large alterations to the broad scale characteristics of the storm circulation but rather had an effect more confined to local features.

Our results suggest that rainfall predictions during ECLs could be improved if accurate eddy resolving SST is used in the model initialisation and integration, providing

other aspects of the initialisation and model parameterisations are also adequate. In particular a special property of the BRAN data, in comparison to most other SST data, is that it is derived from an assimilating ocean model which provides SST patterns that are consistent with multi-variate ocean observations. This 'allows' it to build up complex structures and tight gradients throughout a simulation while also taking advantage of available observational data. The observational data includes sea level height data which provides insight into the depth structure of the ocean eddies. On the other hand, relying on an assimilated simulation rather than a pure observational analysis could produce erroneous features that, while apparently detailed, did not occur in reality. Other SST data, such as from the Group for High-Resolution Sea Surface Temperature (GHRSST 2013) that are derived from satellites, have other limitations. Satellite data see the skin temperature of the ocean which may not be representative of the heat content of the upper ocean. In addition, a loss of data occurs under cloudy conditions and this missing data may be filled in with older data which reduces the accuracy and potentially blurs out complex SST structures. Since the simulations presented here show that localised rainfall and CAPE can be highly sensitive to these structures, they will probably have to be resolved in the SST input data to high resolution numerical weather forecasts for successful prediction to be made of coastal flooding rain in onshore flow.

Past research on the effect of SST gradients on surface winds has shown that convergence tends to occur when air flows from a warm to a cold sea surface (e.g. Sweet et al. 1981). Given this relationship the maximum in CAPE difference seen on the 48 hour average on Fig. 16c along the southern edge of the warm eddy could be explained by a couple of factors. The first is that on the lower level flow trajectory beyond this point (to the south) the CAPE tends to release because the convergence over the strong SST gradient provides sufficient uplift to trigger deep convection. This is consistent with Kuwano-Yoshida et al. (2010) who found evidence of deep convection and thunderstorms preferentially

occurring over strong SST gradients. Under the northwest average flow over the eddy, the southern edge of the eddy has a tendency to be the final point on the trajectory that built up CAPE across the warm eddy, and therefore should have the highest CAPE value. The second influence might be from higher moisture content within a region of moisture convergence forced by the SST gradient. This should increase the dew point temperature that will tend to increase the CAPE (all other factors remaining equal). This complicated process will require further detailed work and analysis.

Overall, a cold pool of air in the middle troposphere moving over a focussed region of warm water is conducive to vertical instability that will be released where there is a convective trigger. This release happens within broad scale storm features such as fronts and rainbands. In addition the simulations suggest that a warm to cold SST gradient can act as this trigger. Given that small ECLs can exhibit widespread convection and warm core characteristics (e.g. Holland et al. 1987), it is worthy of future research to investigate whether these gradients could have broader consequences on the storm evolution. Given the lack of other geographically related triggers offshore, an SST gradient may be the primary non-atmospheric convective triggering mechanism.

6. Conclusions

Simulations have been used to investigate how the distribution of precipitation is related to the distribution of SST during the life cycle of the Australian ECL of 7-9 June 2007. The simulations produce a rain band that is displaced south of the real event and as a result there is a low temporal correlation with the model rainfall when individual station locations are compared. In particular the effect of the introduction of complex eddy and filament structures present in the BRAN SST dataset are considered. In the simulations enhancement of rainfall is found over and downwind of warmer SSTs. Specifically, a large warm eddy present during

this case is associated with a pronounced enhancement of rainfall along its downwind flank where a strong SST gradient exists. An ensemble of three different initialization time simulations shows that these findings are statistically robust. Past research on the effect of SST gradients on surface winds has shown that convergence tends to occur when air flows from a warm to a cold sea surface. In the unstable environment associated with the cold core upper-level low of this case, the simulations suggest that this convergence triggers deep convection and heavy precipitation. The implication is that the SST gradients south of the warm eddy increased the severity of the rainfall in this region. Lightning is concentrated over, and near to, the south of the warm eddy with the greatest number of strikes collocated with the strong SST gradients in this region. The largest CAPE increase occurs on the downwind edge of the warm eddy consistent with the enhanced precipitation region and lower surface pressures. It is concluded that the complex upper ocean heat content structure present during this case significantly influenced the rainfall along and downwind of the warm eddy and strong SST gradients. It is hypothesized that these factors increased the severity and enhanced the localized nature of the storms that impacted the Newcastle area. Overall it is concluded that an accurate eddy resolving SST dataset may be important for accurate forecasts of future storms of this nature.

7. Acknowledgement

This research is funded by Lloyd's Register Foundation (LRF), a UK registered charity and sole shareholder of Lloyd's Register Group Ltd, which invests in science, engineering and technology for public benefit, worldwide. Prasanth Divakaran provided valuable help in working with the BRAN data. The University of Melbourne provided additional financial support for this work. This work forms part of an international research network headed by Prof. Jinyu Sheng of Dalhousie University, investigating extreme marine events.

8. References

Alexander GD Weinman JA Karyampudi VM Olson WS Lee ACL (1999) The effect of assimilating rain rates derived from satellites and lightning on forecasts of the 1993 superstorm. Mon Weather Rev 127:1433-1457

Andrews JC (1979) Eddy structure and the West and East Australian Currents. Flinders Inst Atmos Marine Sci Res Rep 30

Andrews JC Scully-Power P (1976) The structure of an East Australian Current anticyclonic eddy. J Phys Oceanogr 6:756-765

Betts AK (1986) A new convective adjustment scheme. Part I: Observational and theoretical basis. Quart J Roy Meteor Soc 112:677–691

Betts AK Miller MJ (1986) A new convective adjustment scheme. Part II: Single column tests using GATE wave, BOMEX, and Arctic air-mass data sets. Q J R Meteorol Soc 112:693–709

Brassington GB Summons N Lumpkin R (2011) Observed and simulated Lagrangian and eddy characteristics of the East Australian Current and the Tasman Sea. Deep Sea Res 58:559-573

Bridgman H (1985) The Sygna storm at Newcastle-12 years later. Meteorol Aust. 3:10-16

Browning SA Goodwin ID (2013) Large-scale influences on the evolution of winter subtropical maritime cyclones affecting Australia's east coast. Mon Weather Rev 141:2416-2431

Chang, D-E Weinman JA Morales CA Olson WS (2001) The effect of spaceborne microwave and ground-based continuous lightning measurements on forecasts of the 1998 Groundhog Day storm. Mon Weather Rev 129:1809-1833

Christian HJ et al (2003) Global frequency and distribution of lightning as observed from space by the Optical Transient Detector. J Geophys Res 108:4005

Church JA (1987) East Australian Current adjacent to the Great Barrier Reef. Aust J Mar Freshw Res 38:671–683

Cummins KL Murphy MJ (2009) An overview of lightning locating systems: History, techniques, and data uses, with an in-depth look at U.S. NLDN. IEEE Trans Electromagn Compat 51:499–518

Dowdy AJ Mills GA Timbal B Wang Y (2013a) Changes in the risk of extratropical cyclones in eastern Australia. J Clim 26:1403-1417

Dowdy AJ Mills GA Timbal B (2013b) Large-scale diagnostics of extratropical cyclogenesis in eastern Australia. Int J Climatol 33:2318-2327

Dudhia J (1989) Numerical study of convection observed during the Winter Monsoon Experiment using a mesoscale two-dimensional model. J Atmos Sci 46:3077–3107

Evans JL Guishard MP (2009) Atlantic subtropical storms. Part I: Criteria and composite analysis. Mon Weather Rev 137:2065-2080

Fandry CB Leslie LM (1984) A two-layer quasi-geostrophic model of summer trough formation in the Australian subtropical easterlies. J Atmos Sci 41:807-818

GHRSST (2013) Group for High Resolution Sea Surface Temperature. http://www.ghrsst.org Accessed 20 November 2013

Global Climate and Weather Modeling Branch (2003) The GFS atmospheric model. NCEP Off Note 442 http://www.emc.ncep.noaa.gov/officenotes/newernotes/on442.pdf. Accessed 18 October 2013

GPATS (2013) Global Position and Tracking Systems, a revolution in lightning detection and warning technology. http://www.gpats.com.au. Accessed 18 October 2013

Godfrey JS Cresswell GR Golding TJ Pearce AF (1980) The separation of the East Australian Current. J Phys Oceanogr 10:430-440

Griffies SM Harrison MJ Pacanowski RC Rosati A (2004) A technical guide to MOM4. GFDL Ocean Group Tech Rep 5

Hamon BV (1965) The East Australian Current, 1960-1964. Deep-Sea Res 12:899-921

Hart RE (2003) A cyclone phase space derived from thermal wind and thermal asymmetry. Mon Weather Rev 131:585-616

Hobbs PV (1987) The Gulf-Stream rainband. Geophys Res Lett 14:1142–1145

Holland GJ Lynch AH Leslie LM (1987) Australian east-coast cyclones. Part 1: Synoptic overview and case study. Mon Weather Rev 115:3024-3036.

Holton JR (1992) Potential vorticity. In: An introduction to dynamic meteorology, 3rd edn. Academic Press, San Diego pp 97-102

Hong S-Y Noh Y Dudhia J (2006) A new vertical diffusion package with an explicit treatment of entrainment processes. Mon Weather Rev 134:2318–2341

Hopkins LC Holland GJ (1997) Australian heavy-rain days and associated east coast cyclones 1958–92. J Clim 10:621–635

Huang C-Y Raman S (1988) A numerical modeling study of the marine boundary layer over the Gulf Stream during cold air advection. Bound-Layer Meteorol 45:251–290

Janjic ZI (1994) The step-mountain eta coordinate model: Further developments of the convection, viscous sublayer, and turbulence closure schemes. Mon Weather Rev 122:927–945

Jones DA Wang W Fawcett R (2009) High-quality spatial climate data-sets for Australia. Aust Meteorol Oceanogr J 58:233-248

Kuwano-Yoshida A Minobe S Xie S-P (2010) Precipitation response to the Gulf Stream in an atmospheric GCM. J Clim 23:3676–3698

Leslie LM Holland GJ Lynch AH (1987) Australian east-coast cyclones. Part II: Numerical modeling study. Mon Weather Rev 115:3037–3054

Li H Kanamitsu M Hong S-Y Yoshimura K Cayan DR Misra V (2014) A high-resolution ocean-atmosphere coupled downscaling of the present climate over California. Clim Dyn 42:701-714

Li X Zheng W Pichel WG Zou C-Z Clemente-Colón P Friedman KS (2004) A cloud line over the Gulf Stream. Geophys Res Lett 31:14

Liu WT Xie X Niiler PP (2007) Ocean–atmosphere interaction over Agulhas extension meanders. J Clim 20:5784–5797

Maeda Y Yamamoto M Hirose N (2011) Meteorological influences of eddy-resolving ocean assimilation around the cold tongue to the north of the Japanese islands during winter 2004/2005. Asia-Pac J Atmos Sci 47:319-327

McInnes KL Leslie L McBride J (1992) Numerical simulation of cut-off lows on the Australian East Coast: Sensitivity to sea-surface temperature. Int J Climatol 12:783-795

Mills GA Webb R Davidson NE Kepert J Seed A Abbs D (2010) The Pasha Bulker east coast low of 8 June 2007. CAWCR Tech Rep 023

Mlawer EJ Taubman SJ Brown PD Iacono MJ Clough SA (1997) Radiative transfer for inhomogeneous atmosphere: RRTM, a validated correlated-k model for the longwave. J Geophys Res 102:16 663–16 682

Oke PR Brassington GB Griffin DA Schiller A (2008) The Bluelink ocean data assimilation system (BODAS). Ocean Model 21:46–70

Pessi A Businger S (2009) Relationships between lightning, precipitation, and hydrometeor characteristics over the North Pacific Ocean. J Appl Meteorol Climatol 48:833-848

Putrasahan DA Miller AJ Seo H (2013) Isolating mesoscale coupled ocean–atmosphere interactions in the Kuroshio Extension region. Dyn Atmos Ocean 63:60-78

Qi L Leslie L Speer M (2006) Climatology of cyclones over the southwest Pacific: 1992-2001. Meteorol Atmos Phys 91:201-209

Raman S Riordan AJ (1988) The Genesis of Atlantic Lows Experiment: The planetary-boundary-layer subprogram of GALE. Bull Am Meteorol Soc 69:161–172

Ridgway KR Dunn JR Wilkin JL (2002) Ocean interpolation by four-dimensional least squares -Application to the waters around Australia. J Atmos Ocean Tech 19:1357-1375

Rutledge SA Williams ER Keenan TD (1992) The Down Under Doppler and Electricity Experiment (DUNDEE): Overview and preliminary results. Bull Am Meteorol Soc 73:3–16

Schiller A Oke PR Brassington GB Entel M Fiedler R Griffin DA Mansbridge JV (2008) Eddy-resolving ocean circulation in the Asian-Australian region inferred from an ocean reanalysis effort. Prog Oceanogr 76:334-365

Skamarock WC Klemp JB Dudhia J Gill DO Barker DM Wang W Powers JG (2005) A description of the Advanced Research WRF Version 2. NCAR Tech Note 468

Skyllingstad ED Edson JB (2009) Large-eddy simulation of moist convection during a cold air outbreak over the Gulf Stream. J Atmos Sci 66:1274-1293

Small TJ et al (2008) Air–sea interaction over ocean fronts and eddies. Dyn Atmos Oceans 45:274–319

Stammer D (1997) Global characteristics of ocean variability from regional TOPEX/ POSEIDON altimeter measurements. J Phys Oceanogr 27:1743–1769

Sweet W Fett R Kerling J Violette PL (1981) Air-sea interaction effects in the lower troposphere across the north wall of the Gulf Stream. Mon Weather Rev 109:1042-1052

Thiebaux J Rogers E Wang W Katz B (2003) A new high-resolution blended real-time global sea surface temperature analysis. Bull Am Meteorol Soc 84:645-656

Thompson G Rasmussen RM Manning K (2004) Explicit forecasts of winter precipitation using an improved bulk microphysics scheme. Part I: Description and sensitivity analysis. Mon Weather Rev 132:519–542

Trunk TJ Bosart LF (1990) Mean radar echo characteristics during project GALE. Mon Weather Rev 118:459–469

Warner TT Lakhtakia MN Doyle JD (1990) Marine atmospheric boundary layer circulations forced by Gulf Stream sea surface temperature gradient. Mon Weather Rev 118:309–323

Williams ER Geotis SG Renno N Rutledge SA Rasmussen E Rickenbach T (1992) A radar and electrical study of tropical ‘‘hot towers.’’ J Atmos Sci 49:1386–1395

Xie S-P Hafner J Tanimoto Y Liu WT Tokinaga H Xu H (2002) Bathymetric effect on the winter sea surface temperature and climate of the Yellow and East China Seas. Geophys Res Lett 29:2228

You S-H Yoon J-H (2010) High-resolution simulation of the Pacific Ocean. Asia-Pac J Atmos Sci 47:319-327

9. List of figures

10. Tables

Table 1: WRF simulation names, dates, and SST data used.

Case name	Dates	SST data input
Skin	1200 UTC 6 to 0000 UTC 9 June 2007	NCEP skintemp
Control		NCEP realtime
BRAN		BRAN

Table 2: Additional WRF simulation names, dates, and SST data used, for cases with domain 2 initialised 6 and 12 hours after domain 1.

Case name	Date of domain 2 initialization	SST data input
Skin6	1800 UTC 6 June 2007 (6 hours after domain 1)	NCEP skintemp
BRAN6		BRAN
Skin12	0000 UTC 7 June 2007 (12 hours after domain 1)	NCEP skintemp
BRAN12		BRAN

11.Figures

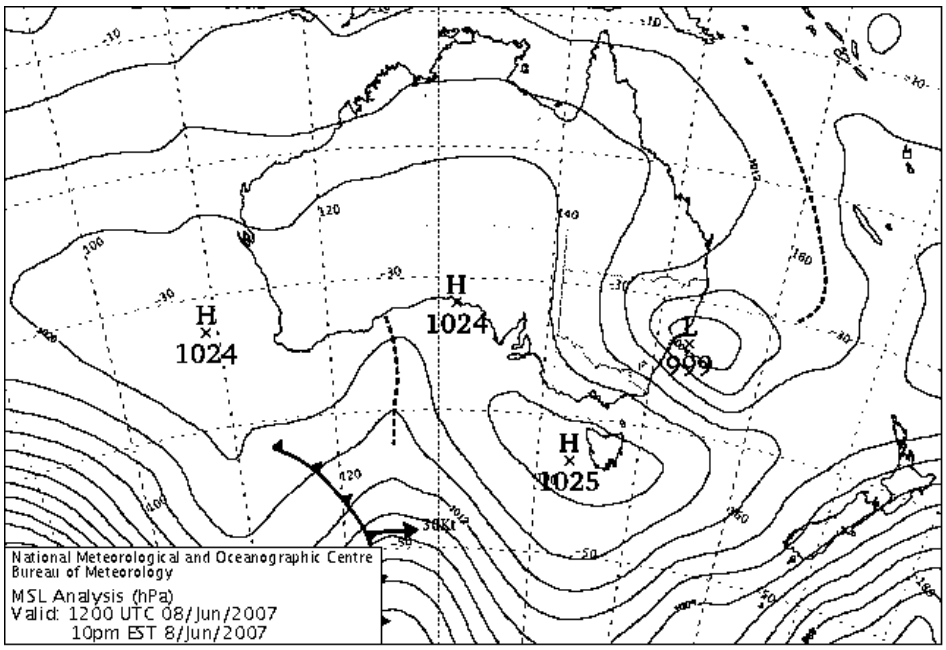

Fig. 1 1200 UTC 8 June 2007 mean sea level pressure analysis from the National Meteorological and Oceanographic Centre, Australian Bureau of Meteorology.

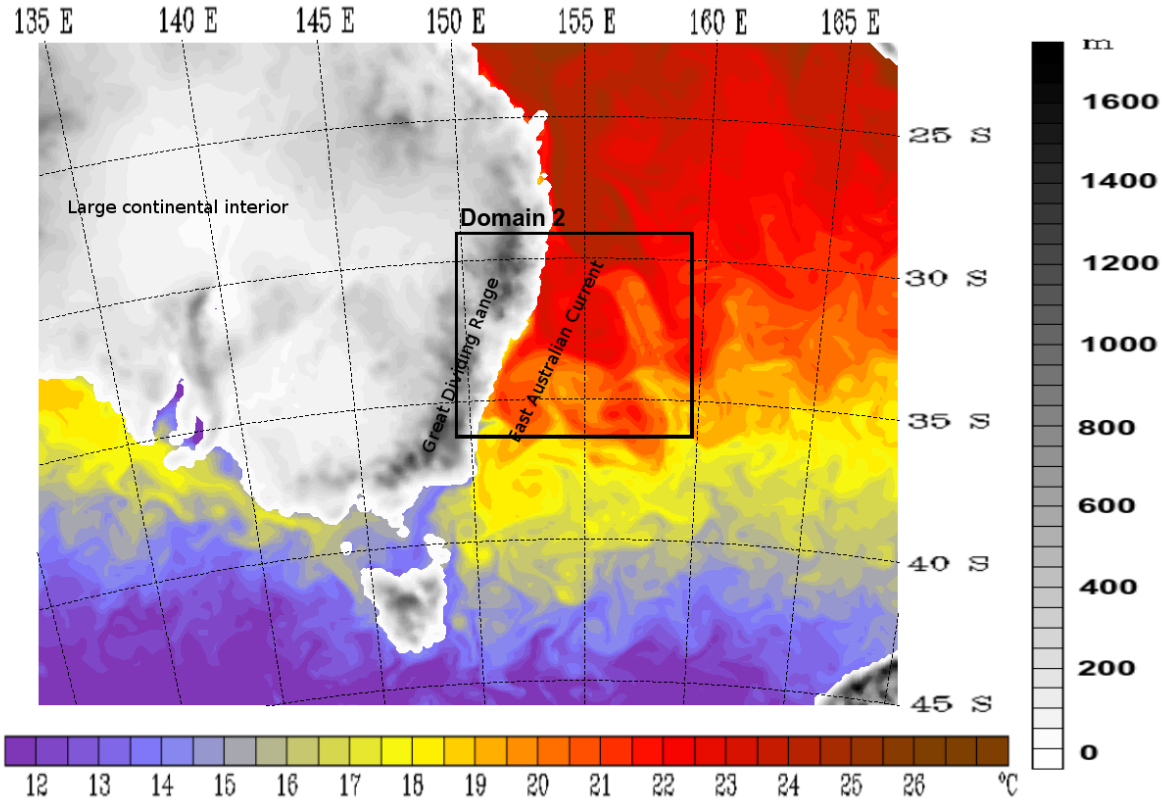

Fig. 2 Domain 1, 15 km (whole map) and domain 2, 3 km (inner box) horizontal resolution WRF domains. Over domain 1, BRAN SST (°C) for 1200 UTC 6 June is plotted in colours and terrain elevation (m) in grey shades.

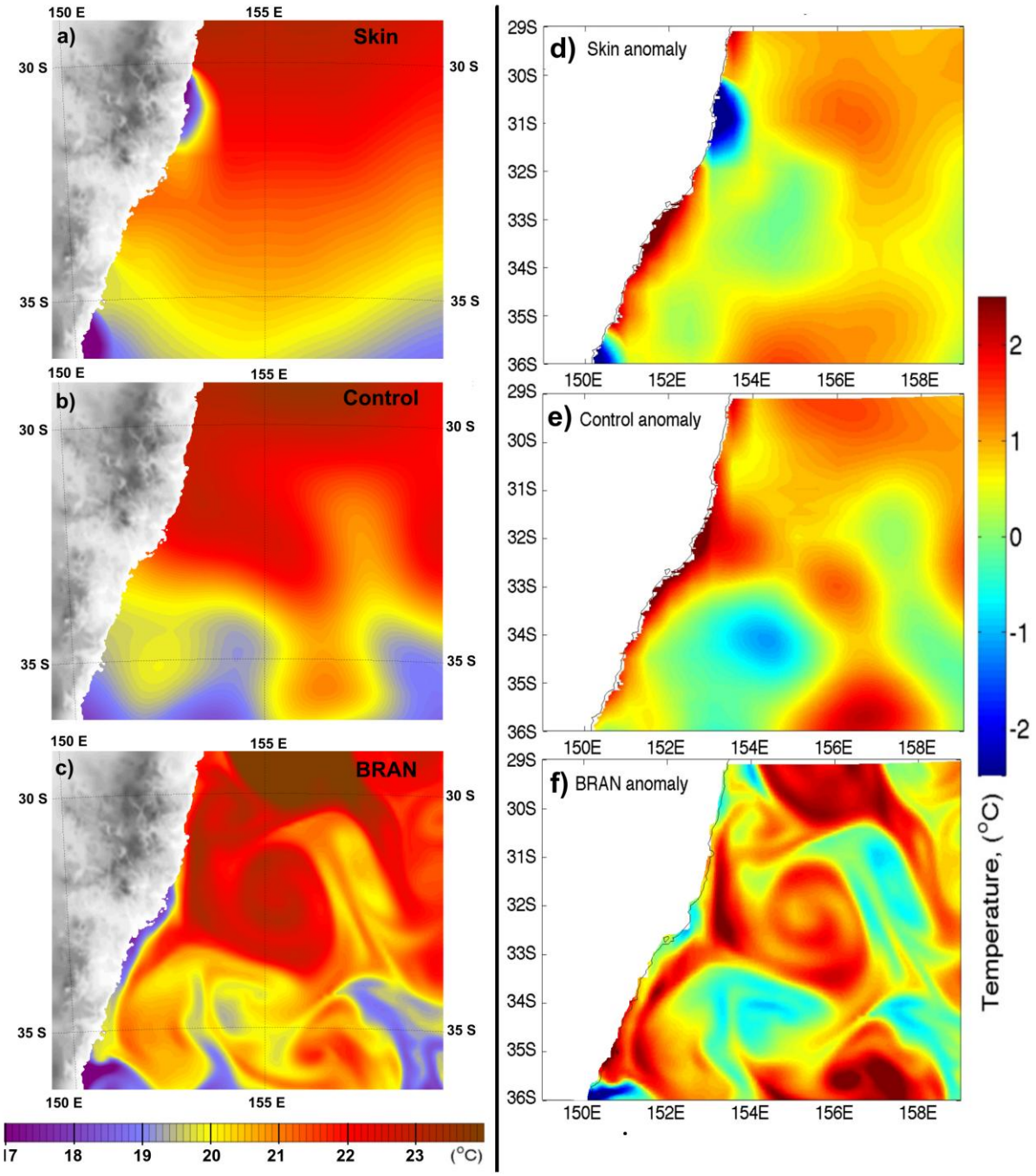

Fig. 3 In the left column are the SST initial conditions (1200 UTC 6 June 2007) for a) Skin, b) Control, and c) BRAN (Schiller et al. 2008). In the right column are the SST anomalies from the CARS climatological SSTs (Ridgway et al. 2002).

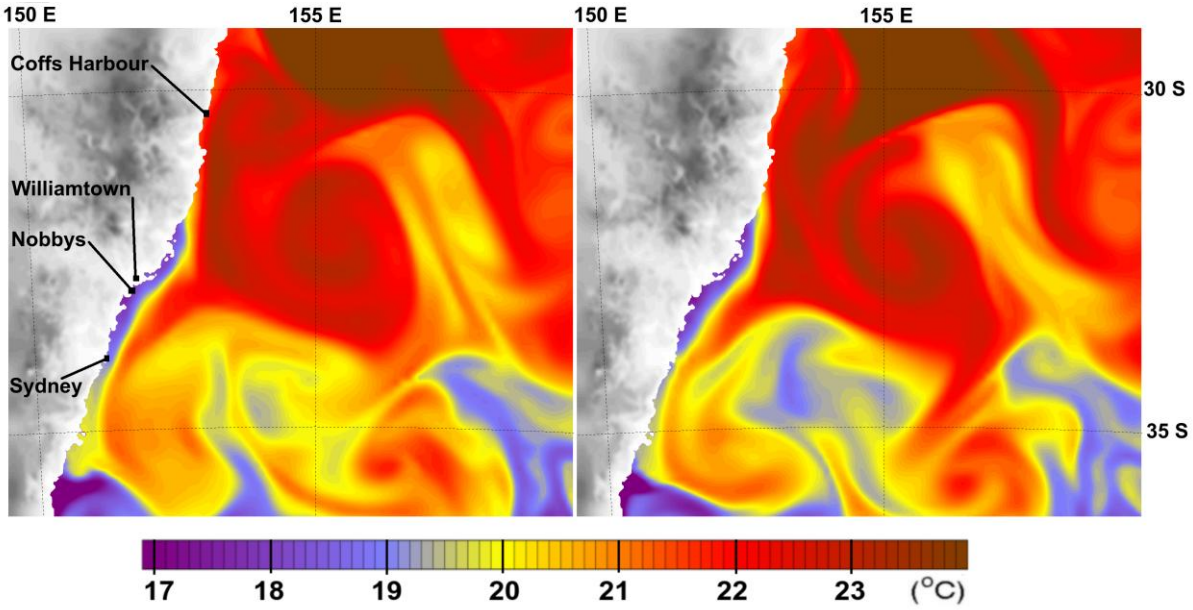

Fig. 4 SST for the beginning (1200 UTC 6 June, left) and end (0000 UTC 9 June, right) of the BRAN simulation. Terrain is shown over land and locations listed in the text are indicated.

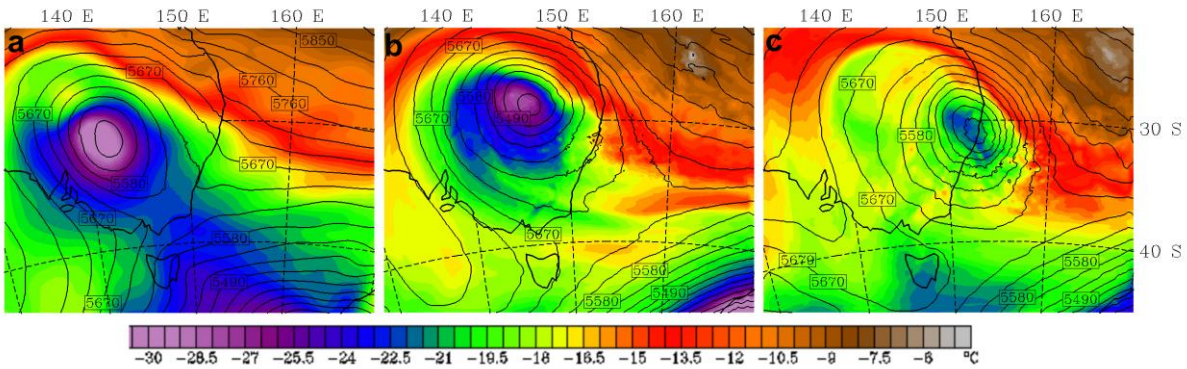

Fig. 5 Domain 1 simulated 500 hPa temperatures (°C, shades) and height (m, contours) at 24 hour intervals for the Control case for a) 1200 UTC 6 June, b) 1200 UTC 7 June, and c) 1200 UTC 8 June.

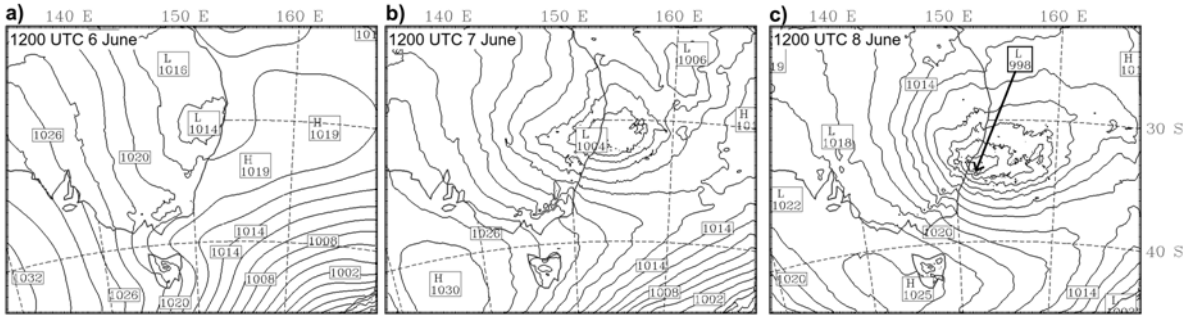

Fig. 6 Domain 1 simulated sea level pressure for the Control case (inverval 2 hPa) for simulation hours 1 (left), 24 (middle), and 48 (right).

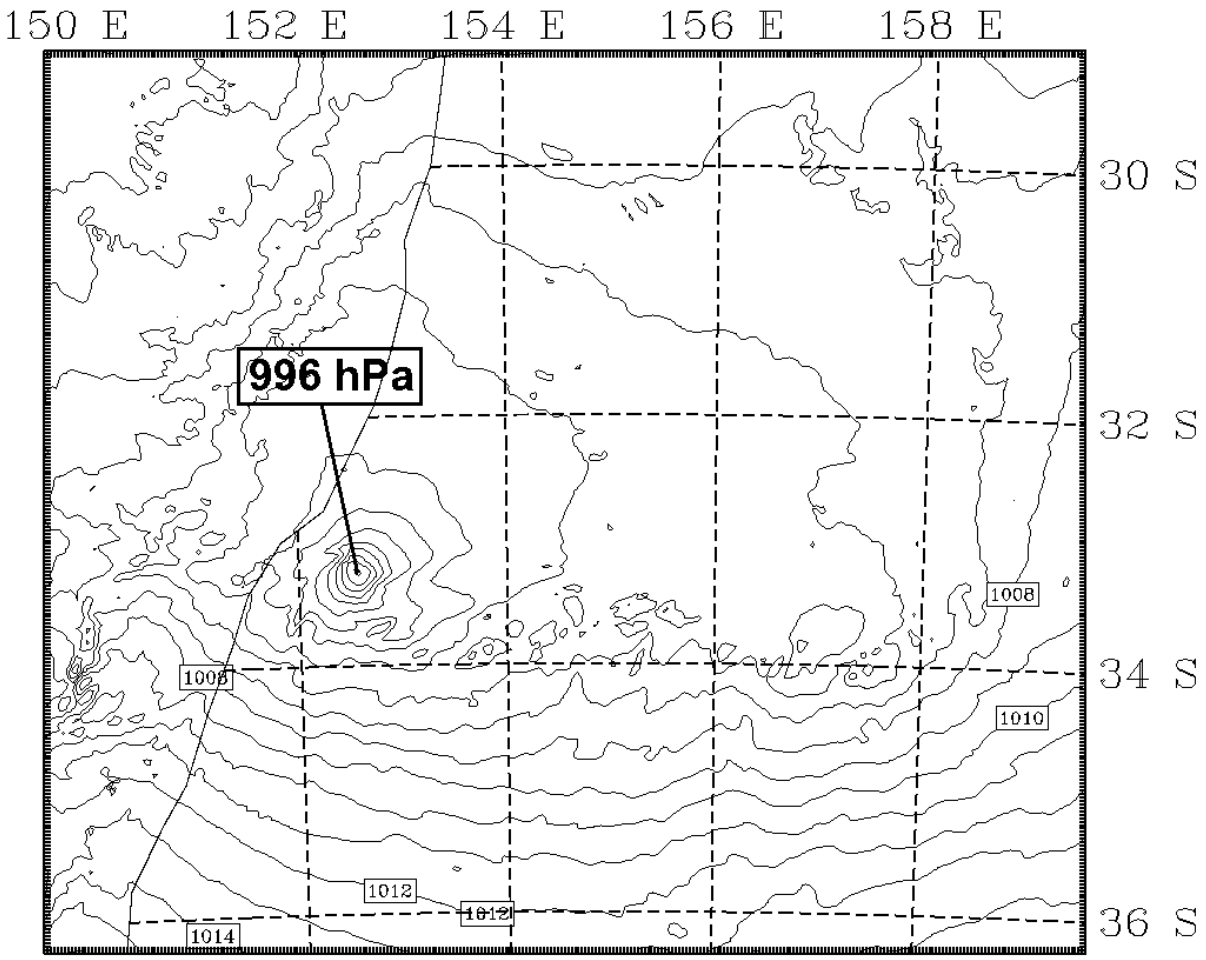

Fig. 7 Sea level pressure (1 hPa intervals) at 0300 UTC 8 June on domain 2 for the Control case.

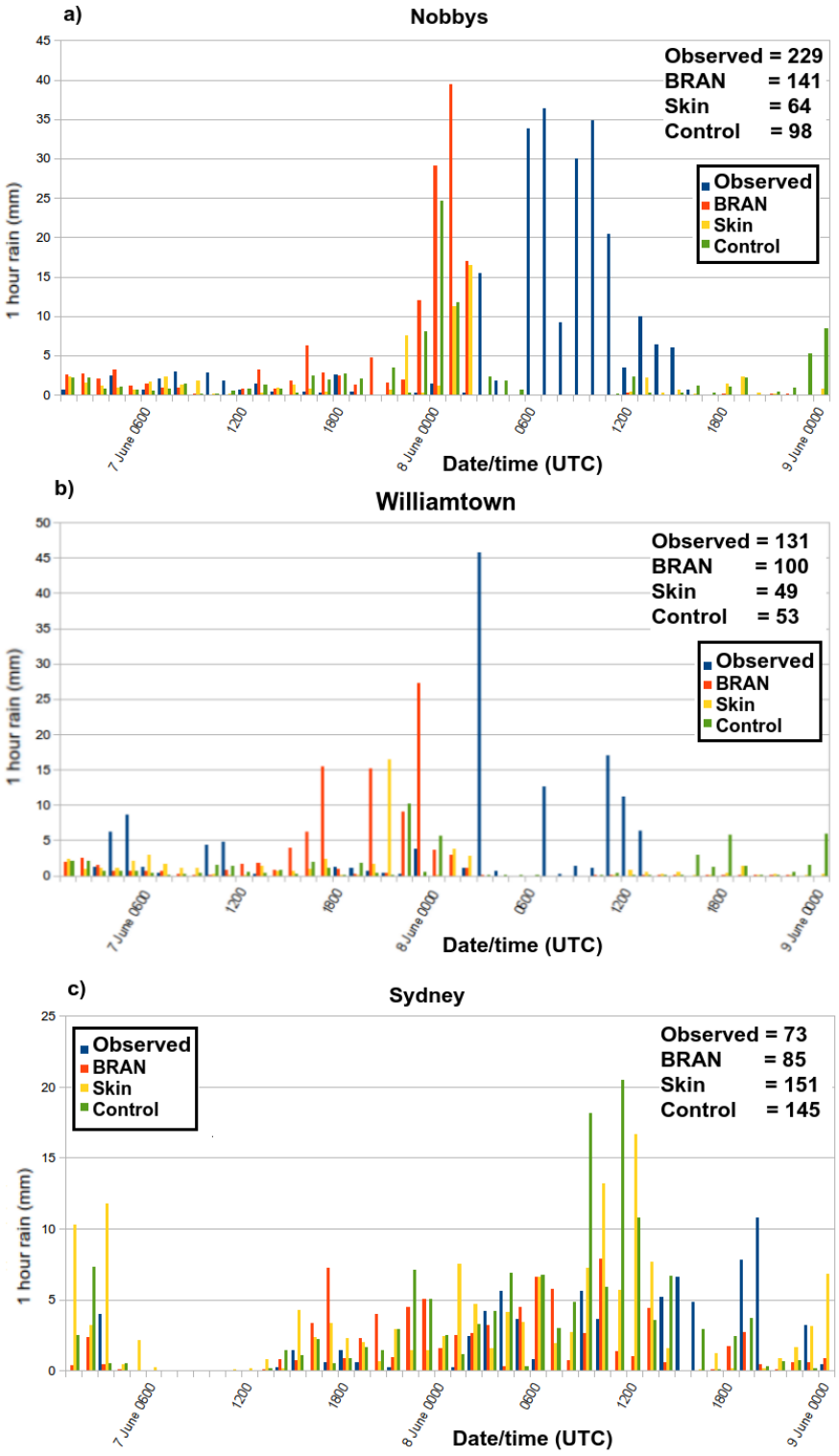

Fig. 8 One hourly total rainfall (mm) for the 48 hour analysis period for a) Nobbys, b) Williamtown, and c) Sydney, compared with the 3 simulations at the same locations. In the top right is the 48 hour total rainfall observed and for each of the simulations.

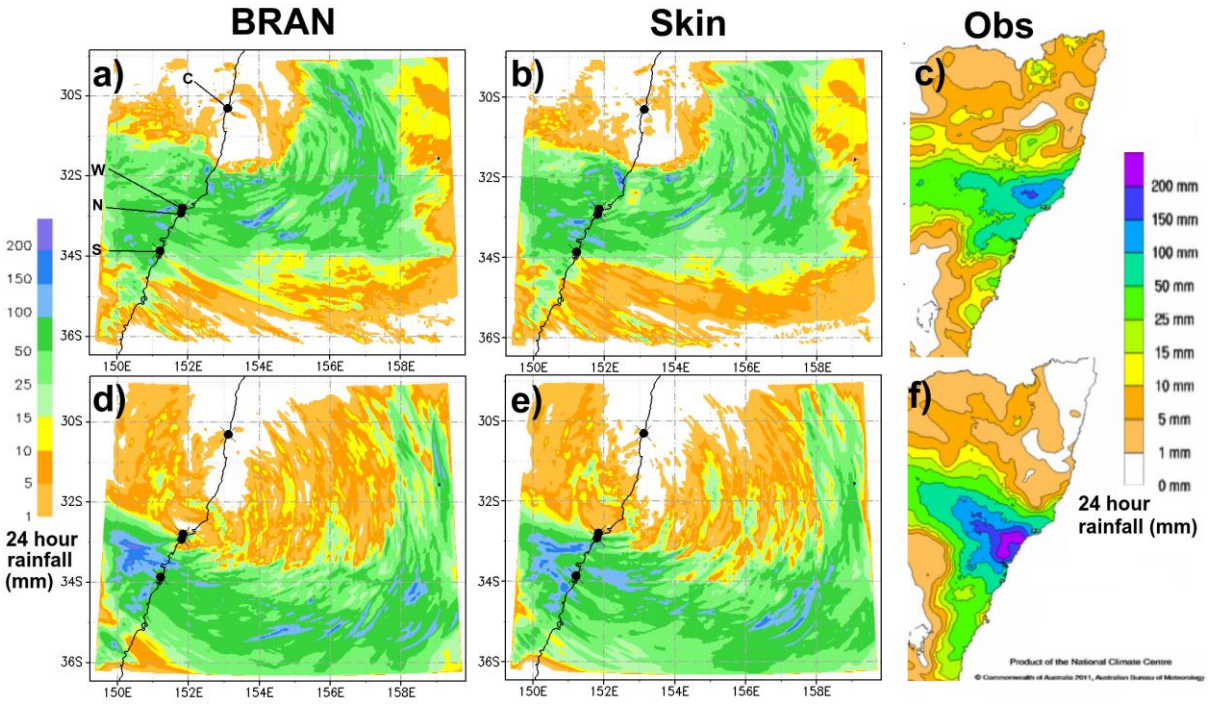

Fig. 9 Comparison of simulated with observed 24 hour rainfall totals (mm). The top row has the 24 hour rain from 2300 UTC 6 to 2300 UTC 7 June 2007 for a) BRAN, b) Skin, and c) observations. The bottom row has the 24 hour rain from 2300 UTC 7 to 2300 UTC 8 June 2007 for d) BRAN, e) Skin, and f) observations. In a) the coastal dot points are the locations of S: Sydney, N: Nobbys Newcastle, W: Williamtown, and C: Coffs Harbour observation stations. The observed plots are a product of the National Climate Centre, Bureau of Meteorology and use the analysis method of Jones et al. (2009).

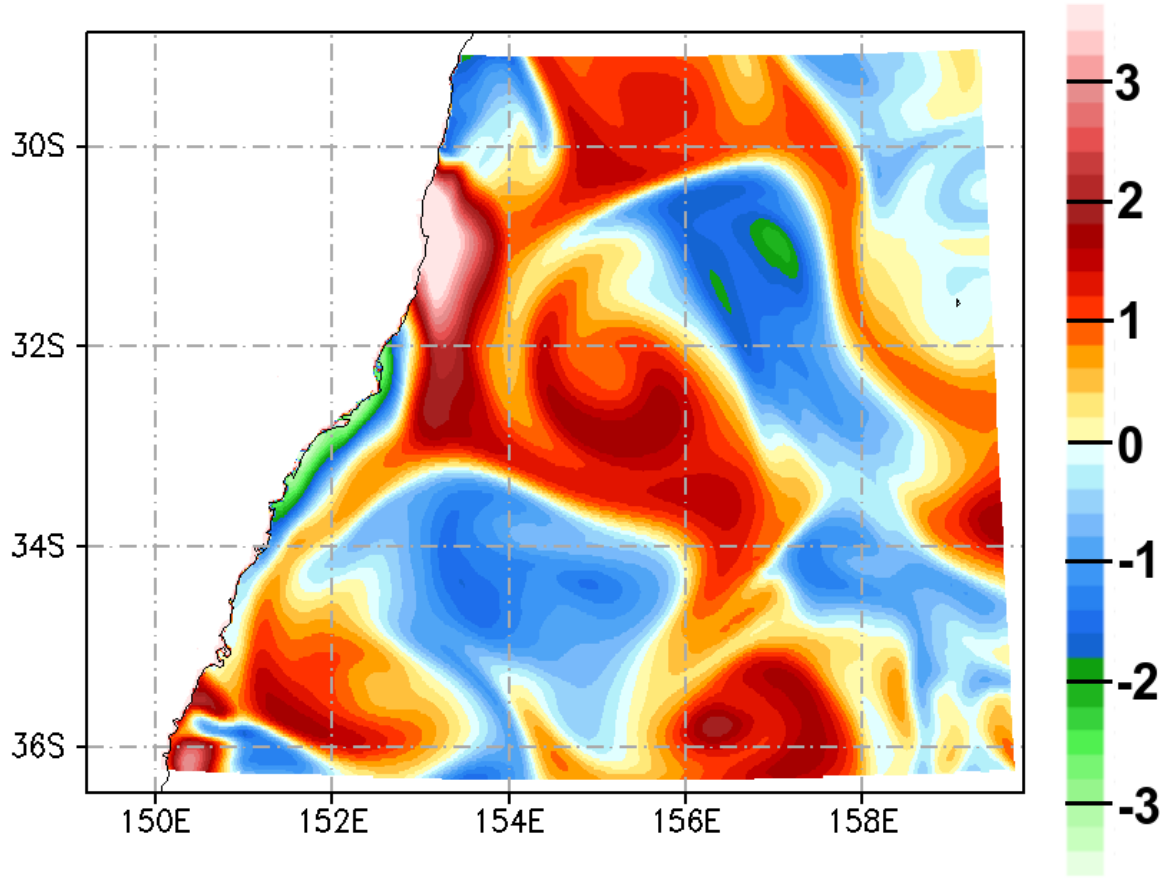

Fig. 10 48 hour (0000 UTC 7 June to 0000 UTC 9 June, 2007) averaged SST difference (°C) between the BRAN and skin temperature datasets (BRAN – Skin).

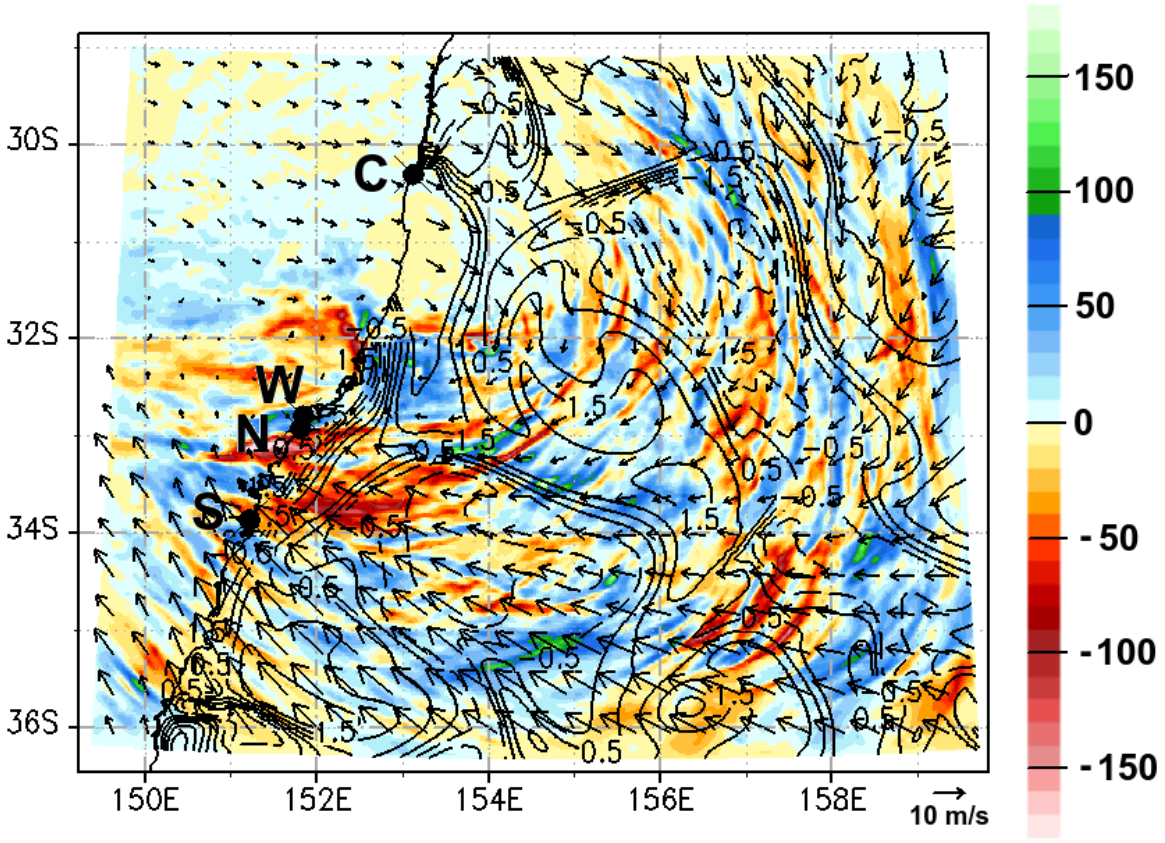

Fig. 11 48 hour (0000 UTC 7 June to 0000 UTC 9 June, 2007) total rainfall differences (colours, mm) (BRAN - Skin). SST differences between the simulations are overlaid for reference as contours at 0.5 C intervals where white contours are warmer, black dashed contours are cooler and the solid black line is the line of no temperature difference (refer to **Fig. 10**). In addition the BRAN simulation 48 hour average 10 metre wind vectors are overlaid as arrows. The coastal dot points are the locations of S: Sydney, N: Nobbys Newcastle, W: Williamtown, and C: Coffs Harbour observation stations.

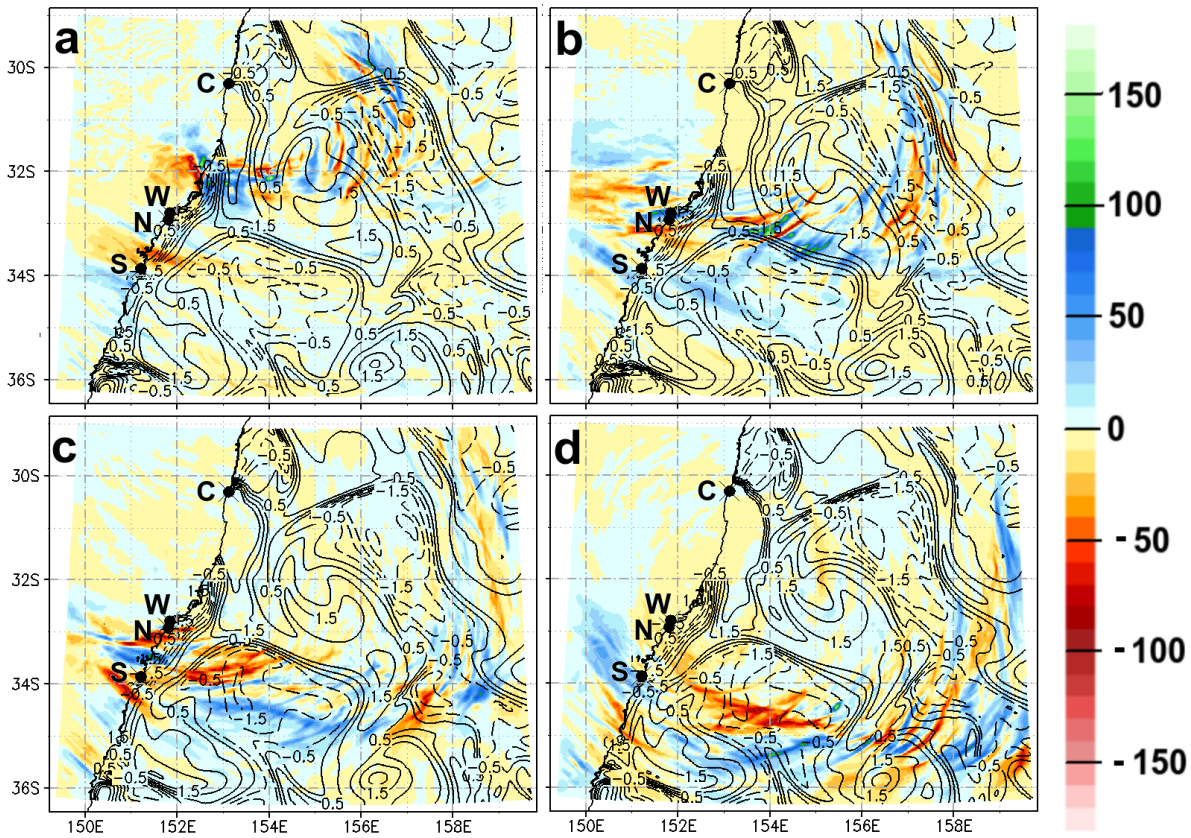

Fig. 12 12 hourly total rainfall difference in colour shades (BRAN - Skin) (mm) and SST difference (black contours °C) for a) 0000 to 1200 UTC 7 June, b) 1200 UTC 7 June to 0000 UTC 8 June, c) 0000 to 1200 UTC 8 June, and d) 1200 UTC 8 June to 0000 UTC 9 June. The coastal dot points are the locations of S: Sydney, N: Nobbys Newcastle, W: Williamtown, and C: Coffs Harbour observation stations.

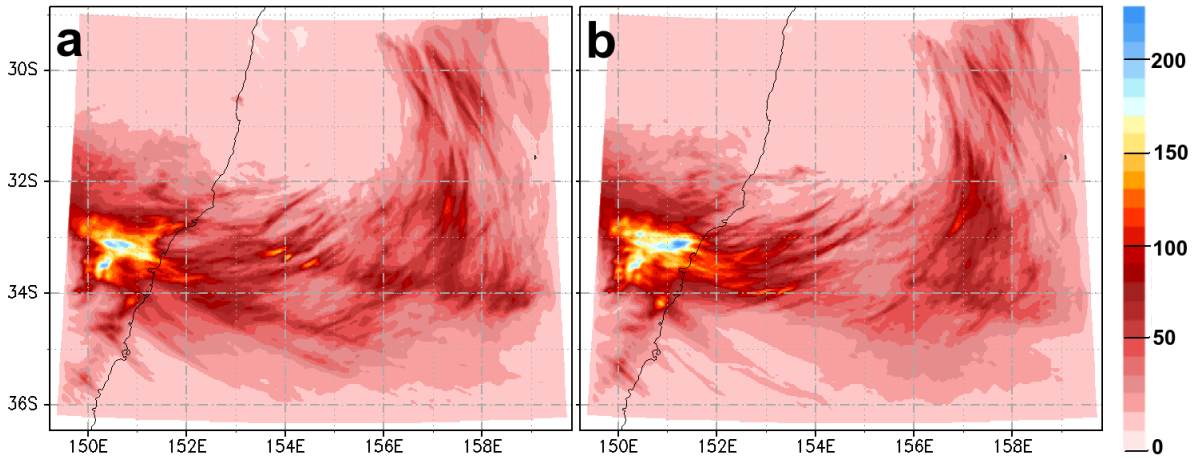

Fig. 13 Ensemble average 48 hour (0000 UTC 7 June to 0000 UTC 9 June) total rain (mm) for a) BRAN and b) Skin.

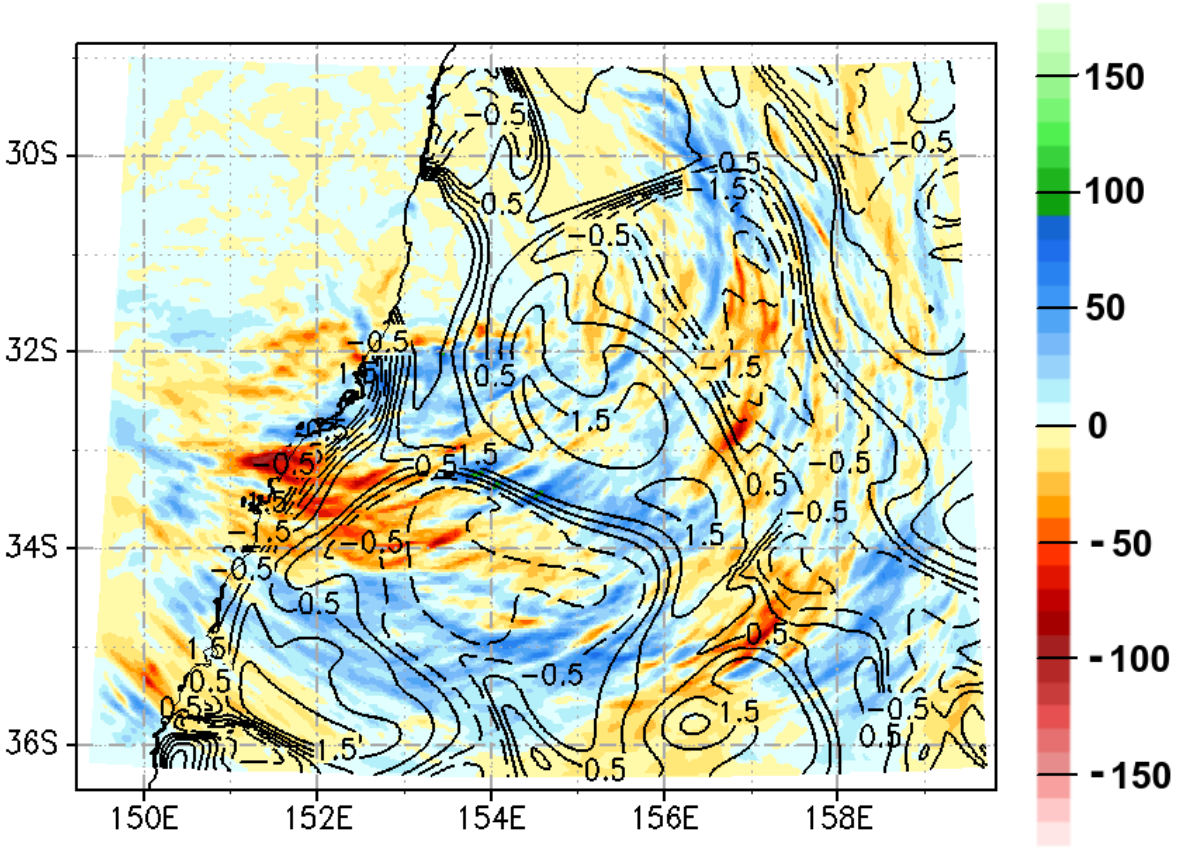

Fig. 14 Ensemble (from 3 runs for each SST initialisation) 48 hour rainfall total differences in colour shades (BRAN – skin temperature runs, mm) with 48 hour SST differences overlaid as contours (°C) for the period shown in Fig. 13.

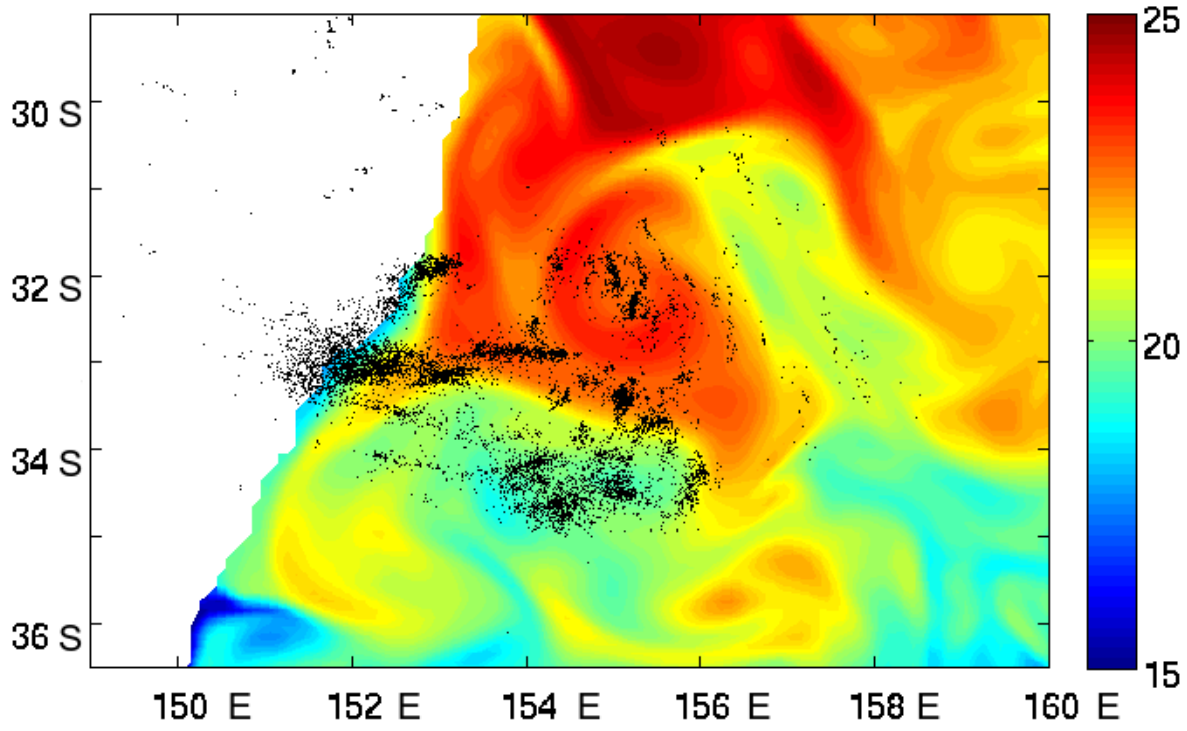

Fig. 15 48 hour (0000 UTC 7 June to 0000 UTC 9 June 2007) Global Position and Tracking System (http://www.gpats.com.au) lightning strikes over the simulation period overlaid on Bluelink SST.

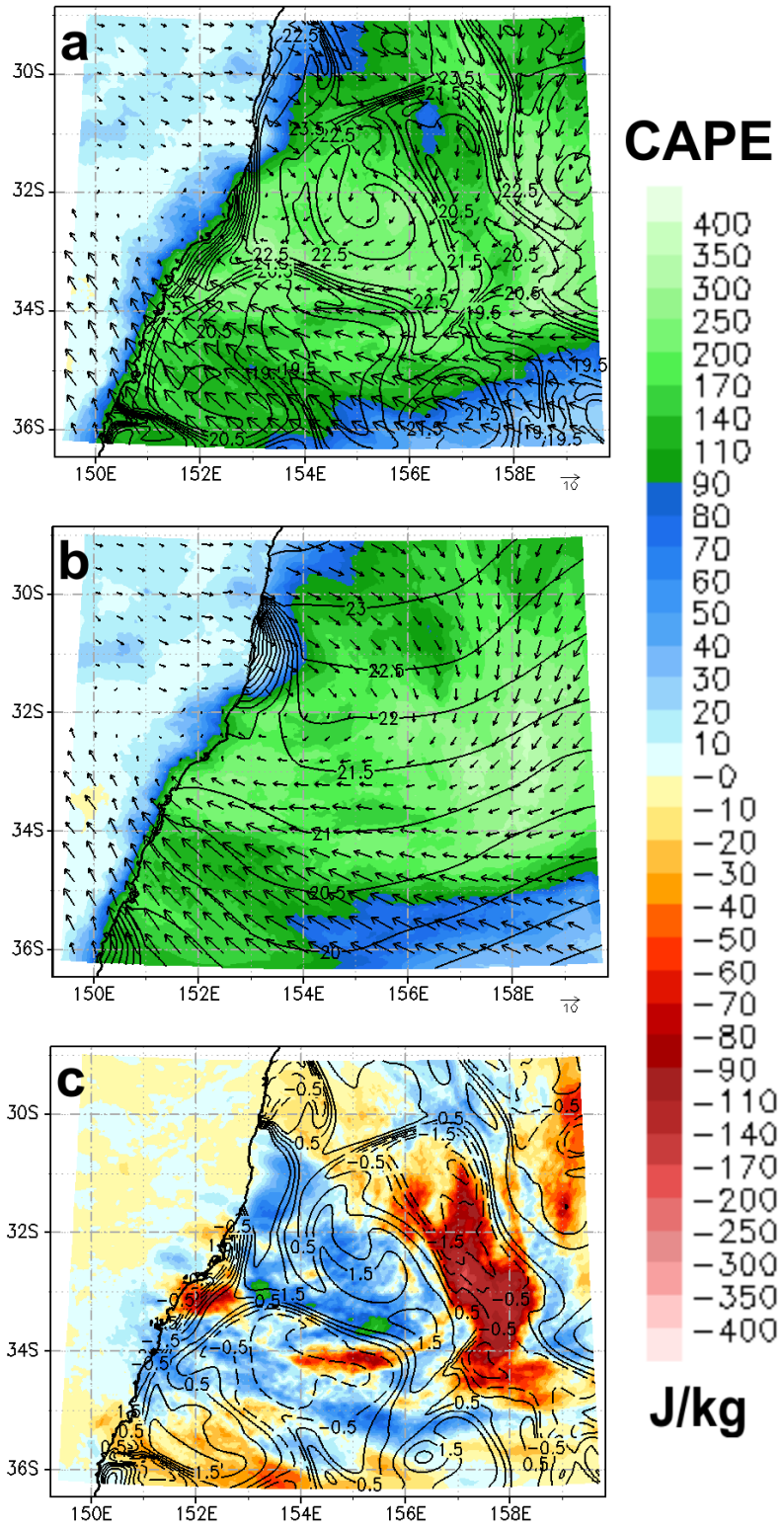

Fig. 16 48 hour average (0000 UTC 7 June to 0000 UTC 9 June, 2007) CAPE (colours, J kg^{-1}) and SST (black contours, °C) and wind vectors (m s^{-1}) for a) BRAN and b) Skin, and c) 48 hour average CAPE difference and SST difference (BRAN - Skin).